Computational Plasmadynamics applied to parametric studies

L Bilbao
INFIP-CONICET, and Physics Department (FCEN-UBA),
Ciudad Universitaria, Pab. I, 1428 Buenos Aires, Argentina

E-mail: bilbao@df.uba.ar

Abstract. A Three-Dimensional Finite Volume Arbitrary Lagrangian-Eulerian simulation code was developed to study different plasma physics problems in 3D+t. The code is based on a complex multi-component species program with transport and radiation terms written and applied to plasma and fusion physics problems. The integration domain is represented with a structured irregular mesh, with fixed connectivity made of hexahedral cells. Coordinates and velocities are assigned to cell vertices. After each calculation cycle, mesh vertices are moved arbitrary over the fluid. The adaptive method consists of shifting mesh vertices over the fluid in order to keep a reasonable mesh structure and increase the spatial resolution where the physical solution demands. The code was a valuable tool for parametric study of different physical problems, mainly optimization of Plasma Focus Machine, detonation and propagation of thermonuclear reactions, and Kelvin-Helmholtz instabilities in the boundary layer of the terrestrial magnetopause.

1. Introduction

A new Arbitrary Lagrangian-Eulerian (ALE) Finite Volume algorithm was developed based on a previously reported code [1]. As in the previous version, Three-Dimensional (3D), time depend, multi-component, two-temperature code was used. A new algorithm for the hydrodynamics was implemented in order to improve the computational efficiency plus the improved capability of adapting the mesh to the solution.

The code includes ion viscosity, thermal conduction (electrons and ions), magnetic diffusion, thermonuclear or chemical reaction, Bremsstrahlung radiation, EOS (from the ideal gas to the degenerate electron gas).

The scope for developing the present numerical method was to perform parametric studies for optimization of several problems in plasma physics. Nowadays there exist several efficient numerical codes in the subject. However the construction of own computational codes brings the following important advantages: (a) To get a deeper knowledge of the physical processes involved and the numerical methods used to simulate them; and, (b) More flexibility to adapt the code to particular situations in a more efficient way than a closed general code would.

In the next paragraph the main improvements will be highlighted.

2. Numerical resolution

We have used an ALE Finite Volume method with hexahedral cells that move at arbitrary velocity. The notation and definition of the geometry is described elsewhere [1]. The main advantage of this method is that the geometry is imposed to the cells and not to the operators.

This method consists of integrating conserved quantities over a cell. For a general fluid property Ψ, the following identity holds

$$\frac{d}{dt}\int_{V(t)}\Psi dV = \frac{\partial}{\partial t}\int_{V(t)}\Psi dV + \oint_{S(t)}\Psi\mathbf{w}\cdot d\mathbf{S} \tag{1}$$

where integration is performed over a cell of arbitrary volume $V(t)$ with boundary $S(t)$ moving at an arbitrary speed $\mathbf{w}$. By choosing $\mathbf{w}=0$, that is both V and S remain fixed, a full Eulerian formulation is retrieved. On the other hand, setting $\mathbf{w}=\mathbf{v}(\mathbf{x},t)$ –fluid velocity- leads to the standard Lagrangian formulation. The adaptive method consists of choosing an appropriated $\mathbf{w}(\mathbf{x},t)$ over the fluid in order to keep a reasonable mesh structure and increase the spatial resolution where the physical solution demands.

For the ideal MHD, the equations for mass (M), momentum ($\mathbf{P}$), internal energy (E), and, magnetic flux (Φ), are

$$\frac{dM}{dt} = \frac{d}{dt}\int_{V(t)}\rho dV = -\oint_{S(t)}\rho(\mathbf{v}-\mathbf{w})\cdot d\mathbf{S} \tag{2}$$

$$\frac{d\mathbf{P}}{dt} = \frac{d}{dt}\int_{V(t)}\mathbf{v}\rho dV = -\oint_{S(t)}\rho\mathbf{v}(\mathbf{v}-\mathbf{w})\cdot d\mathbf{S} - \int_{S(t)}p d\mathbf{S} + \int_{V(t)}\mathbf{j}\times\mathbf{B}\,dV \tag{3}$$

$$\frac{dE}{dt} = \frac{d}{dt}\int_{V(t)}\varepsilon\rho dV = -\oint_{S(t)}\rho\varepsilon(\mathbf{v}-\mathbf{w})\cdot d\mathbf{S} + \int_{S(t)}(\frac{c_p kT}{e}\mathbf{j})\cdot d\mathbf{S} - \int_{V(t)}p\nabla\cdot\mathbf{v}\,dV \tag{4}$$

$$\frac{d\Phi}{dt} = \frac{d}{dt}\int_{\Sigma(t)}\mathbf{B}\cdot d\mathbf{S} = \oint_{C(t)}[(\mathbf{v}-\mathbf{w})\times\mathbf{B}]\cdot d\mathbf{l} \tag{5}$$

where $\mathbf{j}$ is the electrical current density, $\varepsilon = p/\rho(\gamma-1)$ the internal energy density (c_p is the specific heat at constant pressure) and e the charge of the electron. In the last equation Σ is an arbitrary open surface bounded by a closed path C, which moves according to $\mathbf{w}(\mathbf{x},t)$.

The integration domain is represented with a structured irregular mesh, with fixed connectivity made of hexahedral cells. Each cell is surrounded by 6 faces and 8 vertices. Fluid variables are assigned to staggered locations in the mesh. Pressure, internal energy, density, species concentration, cell volume and mass are all assigned to cell centres. Coordinates (x,y,z) and velocities (u_x,u_y,u_z) are assigned to cell vertices.

For example, using $\mathbf{w}=0$ the evolution of the cell mass $M\approx\langle\rho\rangle V$, $\langle\rho\rangle$ being a mean value of the density over de cell, and V the volume, is written as

$$\frac{dM}{dt} = -\sum_i\rho_i\mathbf{v}_i\cdot\mathbf{S}_i \tag{6}$$

where $\mathbf{S}_i$, $\mathbf{v}_i$, ρ_i, are the surface, velocity and mass density of the i-th face of the cell. Analogously, the momentum of a cell, $\mathbf{P}\approx\langle\rho\rangle\langle\mathbf{v}\rangle V$, evolves according to

$$\frac{d\mathbf{P}}{dt} = -\sum_i\rho_i\mathbf{v}_i(\mathbf{S}_i\cdot\mathbf{v}_i) - \sum_i p_i\mathbf{S}_i + \frac{1}{4\pi}(\sum_i\mathbf{S}_i\cdot\mathbf{B}_i)\times\langle\mathbf{B}\rangle \tag{7}$$

where <**B**> is the mean value of the magnetic field on a cell.

Using the same ideas all integral equations are discretized. In order to set the values on the faces, appropriate mean values over adjacent cells are used.

Global conservation of the above magnitudes is checked during calculation. Also, condition *div(***B***)*=0 is controlled over the whole integration domain.

The same method may be applied for more complex modelling of plasmas that includes ion viscosity, thermal conduction (electrons and ions), magnetic diffusion, chemical or thermonuclear reactions, Bremsstrahlung radiation, and realistic equation of state (EOS) from the ideal gas to the degenerate electron gas. The integration in time is sequential. This means that each process is integrated with a different uncoupled method during a time step. The overall truncation error is $O(\Delta x, \Delta y, \Delta z, \Delta t)$. Solution does not dependent on the integration order of the terms.

Calculation proceeds as follows:
- Hydrodynamics is integrated using an improved Predictor-Corrector method as described in the next paragraph.
- Diffusion processes (of species concentration and energy) are integrated with ADI methods (Alternating Direction Implicit) for the 2D/3D case, and with full implicit methods for the 1D case.
- Source terms from chemical or nuclear reactions are explicitly integrated in time.
- Mesh vertices are moved arbitrary over the fluid as it is described below.

2.1. Hydrodynamics

By "*hydrodynamic terms*" we refer only to the Euler equations included into the full set of conservation equations. So in this part of the calculation fluid variables are updated in time assuming that the other processes (diffusion, reaction, convection) are temporally frozen during one time step.

The calculations necessary to advance a solution one step in time Δt are separated in two distinct phases. Phase One consists of an explicit Lagrangian calculation, except mesh vertices are not moved. Phase Two consists of an iteration that adjusts the pressure gradient forces to the advanced time level. This phase eliminates the usual Courant–like numerical stability condition that limits sound waves to travel no further than one cell per time step. In an explicit method pressure forces can be transmitted only one cell each time step, that is, cells exert pressure forces only on neighbouring cells. When the time step is chosen so large that sound waves should travel more than one cell, the one cell limitation is inaccurate and a catastrophic instability develops. To overcome this instability time-advanced pressure gradients may be used. Unfortunately the time–advanced pressures depend on the accelerations and velocities computed from those pressures, so an iterative calculation of the set of equations is required. Physically, iteration offers a means by which pressure signals can traverse across more than one cell in a unit time step.

2.1.1. Phase One, Part One. The velocity components of vertex are explicitly advanced in time using pressure gradients computed from the currently available pressure and mesh coordinates.

2.1.2. Phase Two. The target of this phase is to obtain new velocities that have been accelerated from time-advanced pressure gradients. So this is an implicit problem and iteration must be used. The desired pressure for cell i, must be solution of:

$$p_i^L - f\left(\rho_i^L, \varepsilon_i^L\right) = 0 \qquad (8)$$

Density and internal energy at the time level $n+1$ can be obtained from the values at the time level n with the following iteration

$$\rho_i^L = \rho_i^n \frac{V_i}{V_i^*} \qquad (9)$$

$$\varepsilon_i^L = \varepsilon_i^n + \frac{p_i^n}{\rho_i^n}\left(1 - \frac{V_i^*}{V_i}\right) \tag{10}$$

where V^* is the volume that the cell would have if its vertices were moved using the velocities calculated during Part One.

Finally, a solution for p_i^L can be obtained by applying Newton-Raphson iteration to (8) by performing the following steps:

(a) Compute V^* using the most updated values for the velocity ($\mathbf{v}$).

(b) Compute new guesses for ρ_i^L and ε_i^L with (9) and (10).

(c) Compute a pressure correction δp_i according to

$$\delta p_i = -\frac{p_i^L - f\left(\rho_i^L, \varepsilon_i^L\right)}{S_i} \tag{11}$$

where S_i is a relaxation factor computed once for each cell at the beginning of phase two.

(d) Adjust the current guess for cell pressure

$$p_i^L = p_i^L + \delta p_i \tag{12}$$

(e) Adjust the velocities at the corners of cell i to reflect this pressure change:

The mesh is repeatedly swept and calculations (a)–(e) are performed once for each cell, until no cell exhibits a pressure change violating the inequality:

$$\left|\delta p_i^L / p_{max}\right| < \varepsilon \tag{13}$$

where ε is a suitable chosen small number and p_{max} is the maximum pressure in the mesh.

Phase Two concludes when condition (13) is reached. It can be shown that the number of iterations to reach convergence (N) is approximately:

$$N \approx \left(\frac{u\delta t}{\delta x}\right)\frac{1}{\sqrt{\varepsilon}} \tag{14}$$

where δx is a typical cell dimension. Thus, Phase Two converges in a finite number of iterations, regardless of the actual material sound speed. It is this feature of the ICE method that makes it superior to an ordinary explicit method whose time step must be continually reduced as the sound speed is increased.

2.1.3. Phase One, Part Two. The final values of $\mathbf{v}$ and p obtained from the Phase Two must be used to update vertex coordinates and cell volume and density. In addition cell energy must be accordingly adjusted.

2.2. Mesh rezoning

Lagrangian cell methods are not adequate for describing flows undergoing large distortions, because cells may undergo severe deformations.

Nuclear burning or combustion structures may present steep gradient of temperature, species concentration and heat release. The adaptive method consists of shifting mesh vertices over the fluid in order to keep a reasonable mesh structure and increase the spatial resolution where the physical solution demands.

The rezone velocity $\mathbf{U}$ with which vertices are moved over the fluid is calculated in order to increase spatial resolution where steep temperature gradients and high chemical/nuclear heat release are produced. To do so, a distribution function for vertices concentration is calculated over a 1D

integration path. The new coordinates for each vertex are calculated in such a way that the Lagrangian distance remains uniformly distributed. Another possibility is to define **U** in order to restore an Eulerian method. This calculation of **U** is 1D, where the coordinate represents the path length following one computational direction. The procedure is repeated over several paths where corrections are needed.

Vertex i moves from i to i' according to

$$\mathbf{x}_i' = \mathbf{x}_i + \mathbf{U}\Delta t \tag{15}$$

where **U** is the rezone velocity. During this process there is an exchange of mass, species, energy and momentum among neighbourhood cells.

Then the following steps must be applied
- Calculate the new coordinates using (15), then calculate the volume exchange among neighbourhood cells
- Associated with the volume exchange there will also be a mass, species concentration and total energy exchange. The mass, concentration or energy per unit mass assigned to this volume are computed using a donor cell flux. Finally, fluid conserved properties are updated.
- Once updated the conserved cell and vertex properties, cell volume, density and species concentration are calculated from the new vertex coordinates.

3. Parametric study of a cylindrical pinch

Self-constricted plasma configurations occur in a number of situations, including geophysics (lightning) and astrophysics (current channels at galactic scales). Tonks [2] introduced the term "pinch" to describe these configurations. It was soon discovered however, that the equilibrium pinch suffered from large number of magneto-hydrodynamic instabilities, including sausage and kink instabilities.

Plasma Focus and Z-pinch are machines based on this principle. They are an interesting source of pulsed radiation (including thermonuclear reactions) with a broad utility in many technological applications.

The scope of this study was, on the one hand, to give an approximated description of the scaling law of the thermonuclear reactions in a Plasma Focus (PF) discharge, and, on the other hand, to explore the optimal conditions for generation and propagation of thermonuclear reactions in a cylindrical fibre (Z-pinch).

3.1. Scaling of a Plasma Focus device

The PF dynamics is usually divided into four stages (or phases): breakdown, run-down, convergence and pinch (or focus). A parametric study requires that the code should be run thousand times, In order to speed up the calculation only the last stage is fully modelled, while the previous phases set the initial values for the pinch phase.

Besides the fact that the detailed physics of a PF is rather complicated, the dynamics of the run-down and convergence phases can be reasonably described using simplified models. The "snow-plough" model (SP) assumes that the CS is pushed forward by the magnetic field against a neutral gas [3], the profile is derived from momentum equilibrium and the inner structure is neglected. The SP model assumes that no diffusion of the magnetic field is present, and that the inertia terms are negligible (see, for example [4]). The snowplough model was successfully confronted against both experimental and numerical results (2D plasma fluid codes were available more than 30 years ago [5-6]). In addition, the simplified model used here assumes that a "good" breakdown is produced (that the initial discharge is concentrated in a small volume close to the insulator surface).

The SP model can be used until the travelling profile arrives to the axis (see figure 1). At this point (pinch phase) the SP model is no longer valid, thus the full 2D code is used.
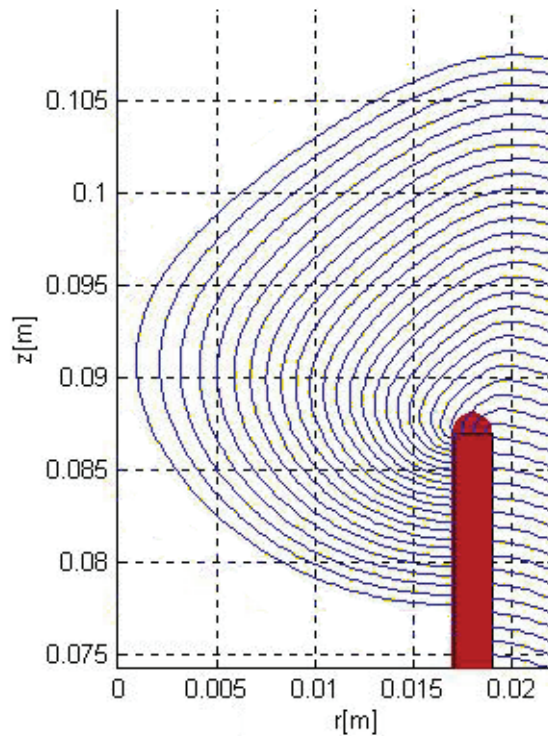
Figure 1. The CS at successive time steps before arriving to the axis ($r = 0$). The inner electrode is also shown. The final step of the snow-plough model is used as the initial condition for the 2D code.

3.2. Pinch stage

During the convergence phase, both the magnetic piston and the shock wave move towards the axis. The pinch phase starts when the shock reflects off the axis. Since the magnetic piston continues its converge, a further compression and heating of the plasma occurs until the reflected shock hits the piston. This stage is usually called "first compression".

Due to the fact that the piston is not a straight cylinder, the maximum compression occurs at different time for different axial positions, leading to the development of an $m = 0$ instability producing several necking (called "second compression" or necking phase).

Nuclear reaction and X-ray emission are produced in the pinch phase. The mechanism of nuclear reaction of a Plasma Focus device remains still unclear. At least three different mechanisms can be devised: thermonuclear production along the whole column as a result of conversion of kinetic energy into internal energy during the first compression, thermonuclear production due to the development of instabilities and further heating (i.e. anomalous resistivity), and beam-target mechanism that can also have different contributions (for example, trapped ions in the pinch or ion beam against the neutral gas). From an experimental point of view some measurements were carried to clarify this point. For example, the anisotropy should be able to differentiate between steady thermonuclear contribution from beam-target or fast moving thermonuclear production. Besides anisotropy there are many other characteristic that are particular for each production: maximum of the neutron production as a function of the filling pressure, scaling with the current, ratio between DD and DT outputs, influence of contaminants, etc. Probably the above mentioned three mechanisms may share one or more of these properties, but quite probably they can not share all the same properties.

3.3. Pinch simulation

In order to get reasonable initial conditions for the compression stage, a simplified snow-plough model was used for reproducing the coaxial and convergence stage. In figure 1, the CS at successive time

steps during the convergence stage is shown. The corresponding current at the final time of the convergence is taken as the initial current for the compression.

For the pinch stage a 2D, time dependent, two-fluid (ions and electrons), two-temperature, model was used. This set of equations was coupled to the circuit equation that represents the main discharge of the device, through

$$\frac{d[(L_o + L_b)I]}{dt} = \frac{Q}{C} - RI - \int_b d\mathbf{l} \cdot \mathbf{E}' \tag{16}$$

where Q is the charge of the capacitor bank, C the capacity, Lo and R the inductance the resistance of the (concentrated) circuit, respectively, L_b the inductance calculated at the plasma boundary (b refers to the plasma boundary) and I the current.

In order to characterise the neutron production of the first compression thousands of runs changing the initial parameters must be performed.

We have used data from 5 different Plasma Focus, namely, PFII (BA), Nessi (NE), Speed (SP), Frascati (FR) and Brasimone (BR). The main parameters are (see table I): anode length l and radius a, cathode radius b, bank capacity C, external inductance L_0, charging voltage V_0, initial filling pressure (p_0) and the gas type (only pure D_2 were used in the present calculations). These machines were selected because they cover an ample range of energy and velocity, and results from them are readily available in the literature. The Brasimone Plasma Focus is the solely one that worked in a repetitive fashion.

Table 1. List of parameters (a: inner radius, b: outer radius, l: anode length, C: bank capacity, L_o: external inductance, V: charging voltage).

Case	a(cm)	b(cm)	l(cm)	$C(\mu F)$	L_0(nH)	V(kV)
BA	1.8	3.6	12.	10.5	31.	20÷40
NE	3.3	6.25	21.	225.	20.	15÷25
SP	2.5	7	6.5	1.56	40.	120÷220
FR	8.	12.	56.	1250.	16.	20÷40
BR	1.65	4.5	13.5	30.5	100	21

The calculations proceed as follows. For each case and for each possible value of V_0 the initial filling pressure is browsed until the maximum neutron yield is obtained.

In figure 2 the calculated neutron output (Y_n) is plotted as a function of the pinch current. The best fit is given by

$$Y_n = 6 \times 10^9 \ I_p^4 \tag{17}$$

that corresponds fairly well to measured values. Also the neutron output is plotted as a function of bank energy in figure 3. Note that at higher energies Plasma Focus devices are less efficient since the ratio between the output energy (proportional to the thermonuclear yield) and the input energy (electrical energy) diminishes with bank energy.
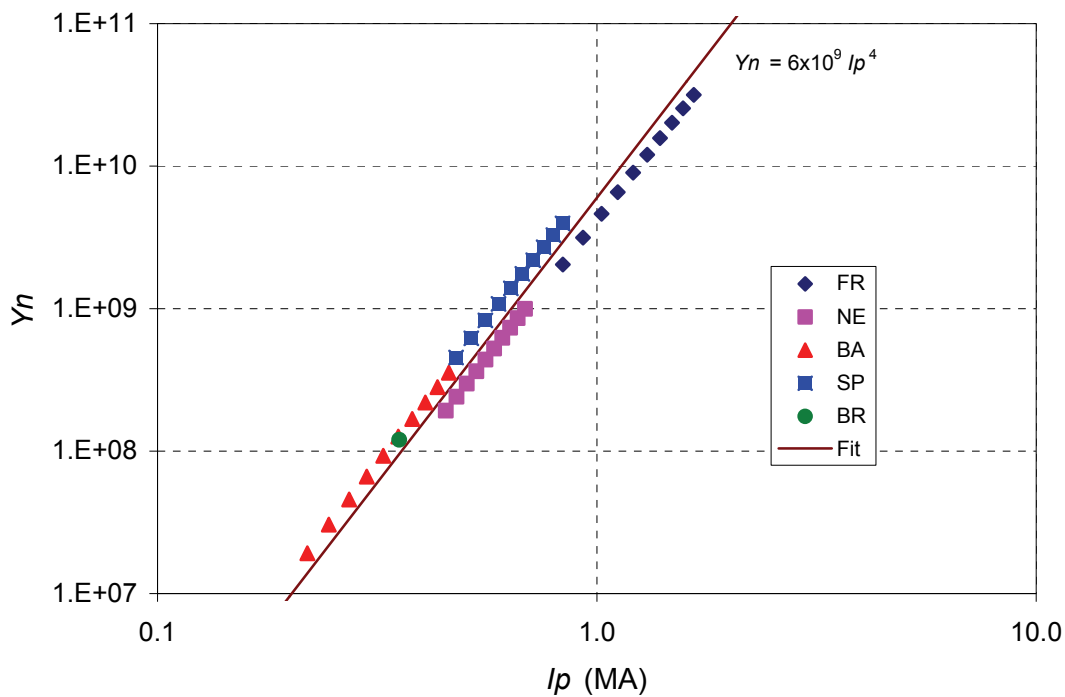
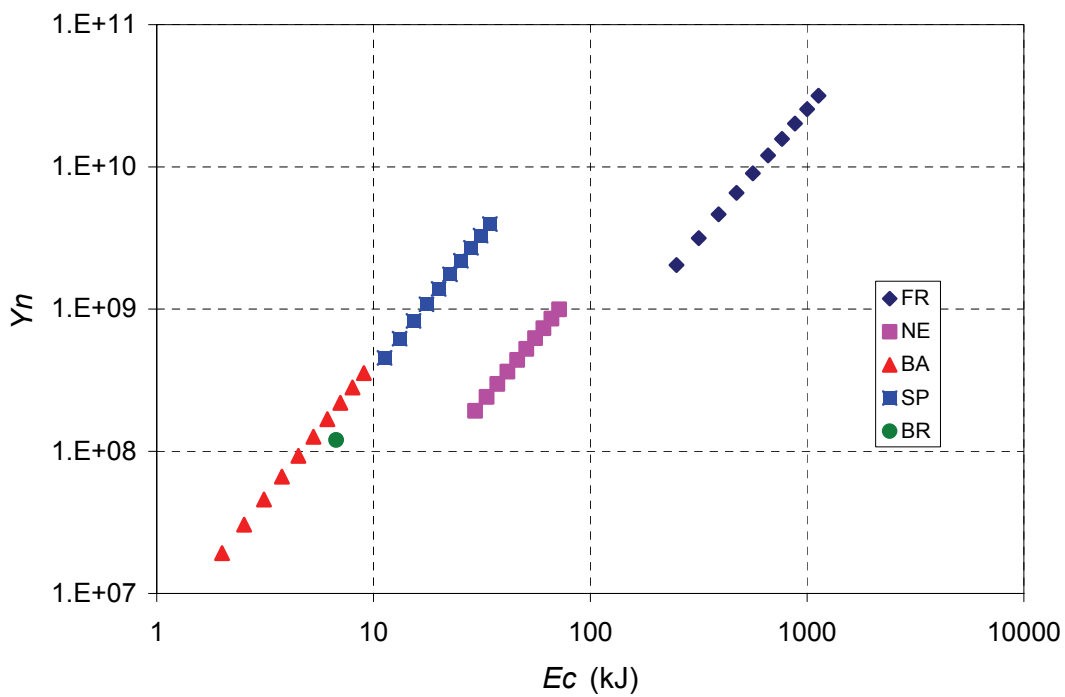**Figure 2.** Neutron production (Y_n) vs. pinch current (I_p).

Figure 3. Neutron production (Y_n) vs. bank energy (E_c).

In order to clarify this behaviour, in figure 4 the ratio between ion and electron temperature at the end of the first compression phase are plotted against the energy. During convergence and

compression the ions are heated by a shock wave, while electrons are heated by collisions with atoms (joule heating is less important before the development of instabilities). From figure 4 it is apparent that at high energies the equipartition time is relatively smaller than the obtained at low energies, thus the ions are expected to be relatively cooler. This means that high energy machines are less efficient in neutron production than smaller machines. This fact seems to be linked to the necessary relation, set by construction, between the parameters that prevents to optimize all stages at the same time.
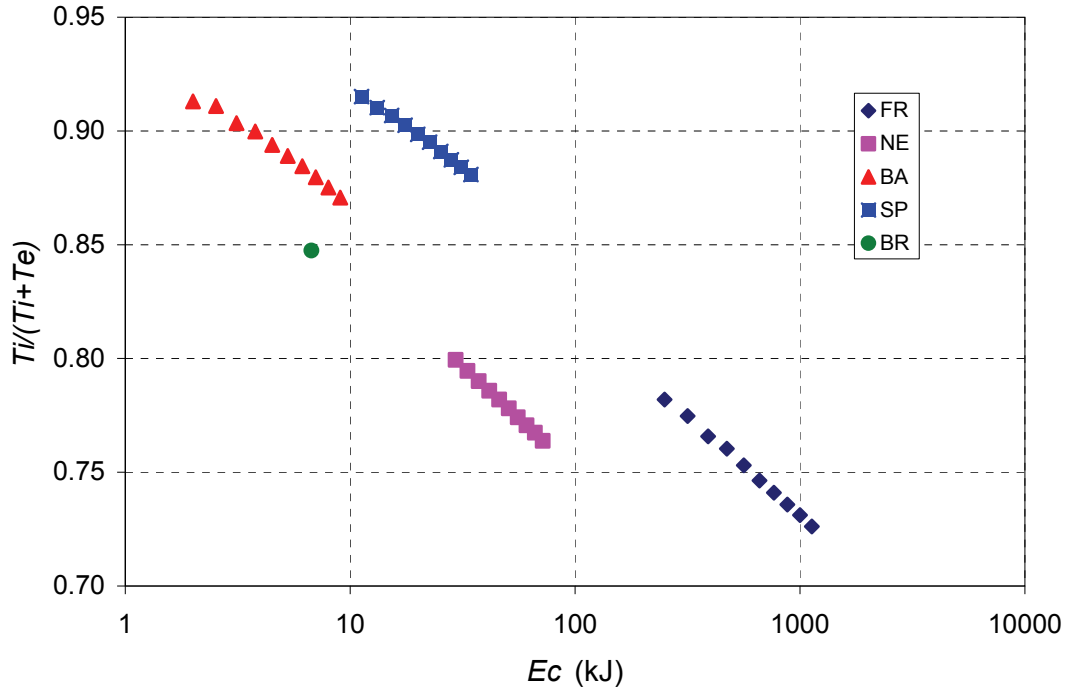

Figure 4. Temperature ratio (T_i/T_i+T_e) vs. bank energy (E_c)

3.4. Pinch analysis
The numerical 2D simulation was a useful tool for the parametric study of a Plasma Focus. The numerical simulation helped to understand the important role of the equipartition time on the neutron production. It is apparent from these results that larger machines are less efficient than smaller ones.

The cooling effect of the equipartition time has not to be confused to the drastic drop in neutron production that happens at higher energies. A possible explanation, based on the results from the 2D code, is that assuming that "good" and "bad" breakdown regions are separated by the line $p_o \propto V_o$ [7] then always will be "crossed" by the pressure of maximum production, $p_o \propto V_o^2$, at higher energies. This behaviour is confirmed by the present parametric study, which means that the standard PF configuration cannot be simultaneously optimized for breakdown and nuclear production.

4. Generation and propagation of thermonuclear reactions.
The idea of a simple nuclear reactor based on a Z-pinch has been discarded because the heating of a whole plasma column to high temperatures will require unrealistic energy input for the plasma heating [8-11]. Another approach [12] to the production of a positive energy yield consists of a small pinch zone heated to high temperature only. Experiments on Z-pinches always concern low and high temperatures and high-density plasma regions that arise spontaneously in Z-pinch necks. A burn wave might be initiated in the Z-pinch column if in one of this small plasma region a Lawson-like condition

is fulfilled. The nuclear energy, which is produced because of a burn wave spread, is controllable and is sufficient for the compensation of energy losses for the pinch production.

Perhaps the most promising application of liner implosions is the volume or spark ignition in cylindrical plasma. During the last decade fast implosions of annular current sheaths (fast Z pinches) have made important progress in reaching high energy densities. New possibilities for a broad spectrum of experiments, from X-ray generation to controlled thermonuclear fusion are devised. At present Z pinches are the most intense laboratory X-ray sources; powers in excess of 200 TW have been obtained [13,14].

At the same time experiments have shown [15,16] that a cylindrical liner can successfully confine a magnetised, hot plasma column [17]. The technical parameters necessary for Inertial Confinement Fusion (ICF) applications (in particular, volume and spark ignition in plasma compressed by an imploding liner) have been investigated through numerical simulations. These calculations provide an insight into the structure of the liner and the plasma and indicate the range of parameters required for ignition and detonation in such a liner-pinch system.

Simple 2D simulations of a D-T nuclear detonation inside a cylindrical liner have been performed by Avrorin *et al* [18].

In order to find the ignition criteria and the correct structure it is necessary to perform two-dimensional numerical simulations using a realistic plasma fluid model and corresponding transport coefficients.

The system of equations is based on a two-fluid model of plasma with transport and viscosity coefficients used in [19] and the fusion cross sections from [20].
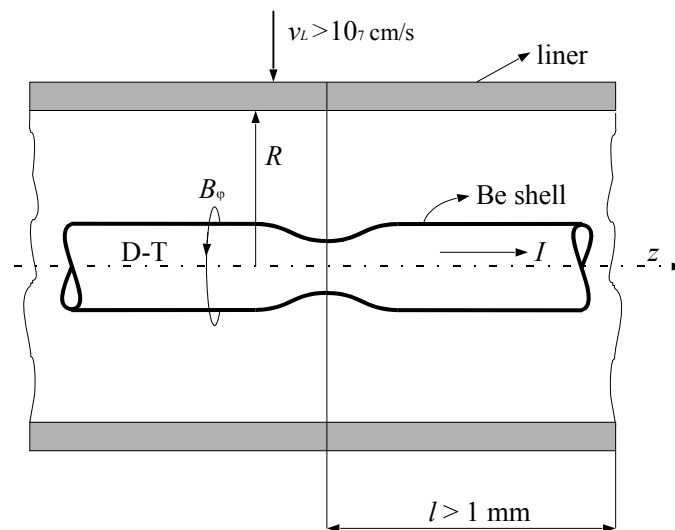

Figure 5. Implosion of cylindrical liner on a Z-pinch.

A promising approach is based on a spark created in a neck of a dense Z-pinch. The neck is formed as a result of an $m = 0$ instability starting from an initial small $m = 0$ axial perturbation. The advantage of this approach is that the spark can be programmed to occur at the moment of maximum pinch current at the correct place and time by choosing suitable initial configuration. The disadvantage is that one must provide an initial magnetic flux and the associated current I_0 and that the current rise time t_r must be short, in most cases $t_r < 10$ ns. Considering the short t_r's required, it seems that the direct use of present day megampere generators [13,14] is inadequate and the only possible means for getting $dI/dt = 10^{15}$ A/s is the compression of a B_φ-flux of a Z-pinch by a fast imploding liner (figure 5).

The spark created in a neck of a dense Z-pinch can ignite a fusion detonation in the adjacent D-T plasma channel. An $m = 0$ instability of a Z-pinch carrying a current of the order of 10 MA, with a rise

time inferior to 10 ns can generate a spark capable of igniting a fusion detonation in the adjacent D-T plasma channel. Such µZ-pinch may be produced by a fast implosion of a cylindrical liner, while a conical channel properly chosen can amplify the spark energy. In order to derive some general rules for the parameters of the spark, the transition, the cylinder of advanced fuel and the liner different numerical models were used.

In the following example, the initial pinch parameters are: radius $a = 0.2$ cm, temperature $T = 30$ eV, linear density $N = 5.2 \times 10^{19}$ part/cm.

Different liner mass and velocity were used. Also, we have used several initial velocities for the liner ranging from slow liners ($v = 2 \times 10^6$ cm/s) to fast liners ($v = 3 \times 10^7$ cm/s). The initial current was $I = 1$ MA.
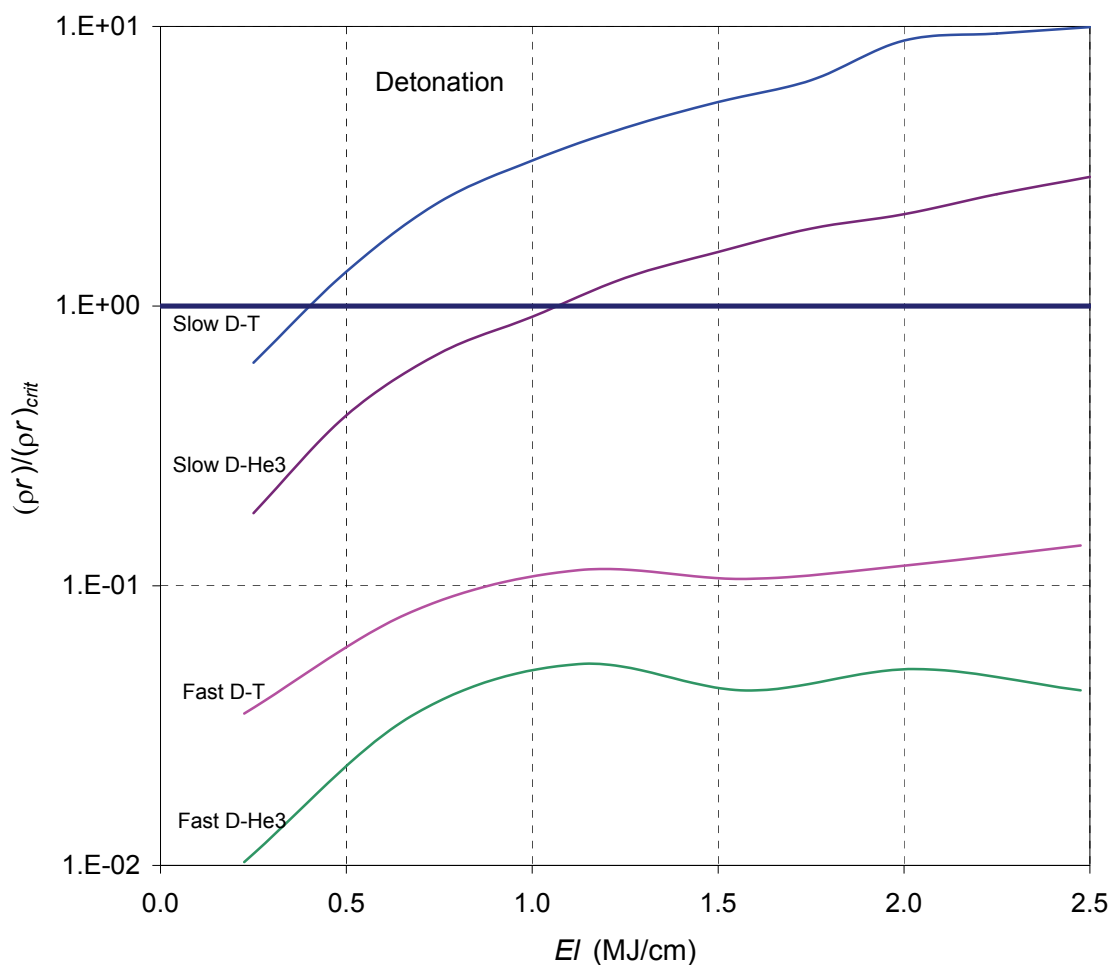

Figure 6. Detonation criteria for slow and fast liner for D-T and D-He3 plasma. Fast liners do not provide enough inertia to confine the plasma up to the detonation conditions.

Note that at the same kinetic energy value of the liner, the slow one provides a larger tamping effect than the faster one, while the faster one produces a larger temperature rise in the pinch than the slow one.

In D-T the condition for detonation propagation is fulfilled at 0.5 MJ/cm liner kinetic energy level (see figure 6). D-He3 plasma requires liner energies above 1.1 MJ/cm in order to reach detonation conditions.

Although the detonation propagation condition is achieved at about 0.5 MJ/cm of liner energy (figure 6), the trigger energy necessary for starting the burn is higher than the required in the previous case. For D-D ignition is obtained at the level of 1.3 MJ/cm, while for D-He3 the ignition criterion seems to be impossible to reach within reasonable liner kinetic energy. Note that, the fast liner produces a larger temperature in the plasma (see figure 7). This has the effect of increasing the thermonuclear output that inhibits a large compression. For this reason both the detonation and ignition are hardly to reach using fast liners.
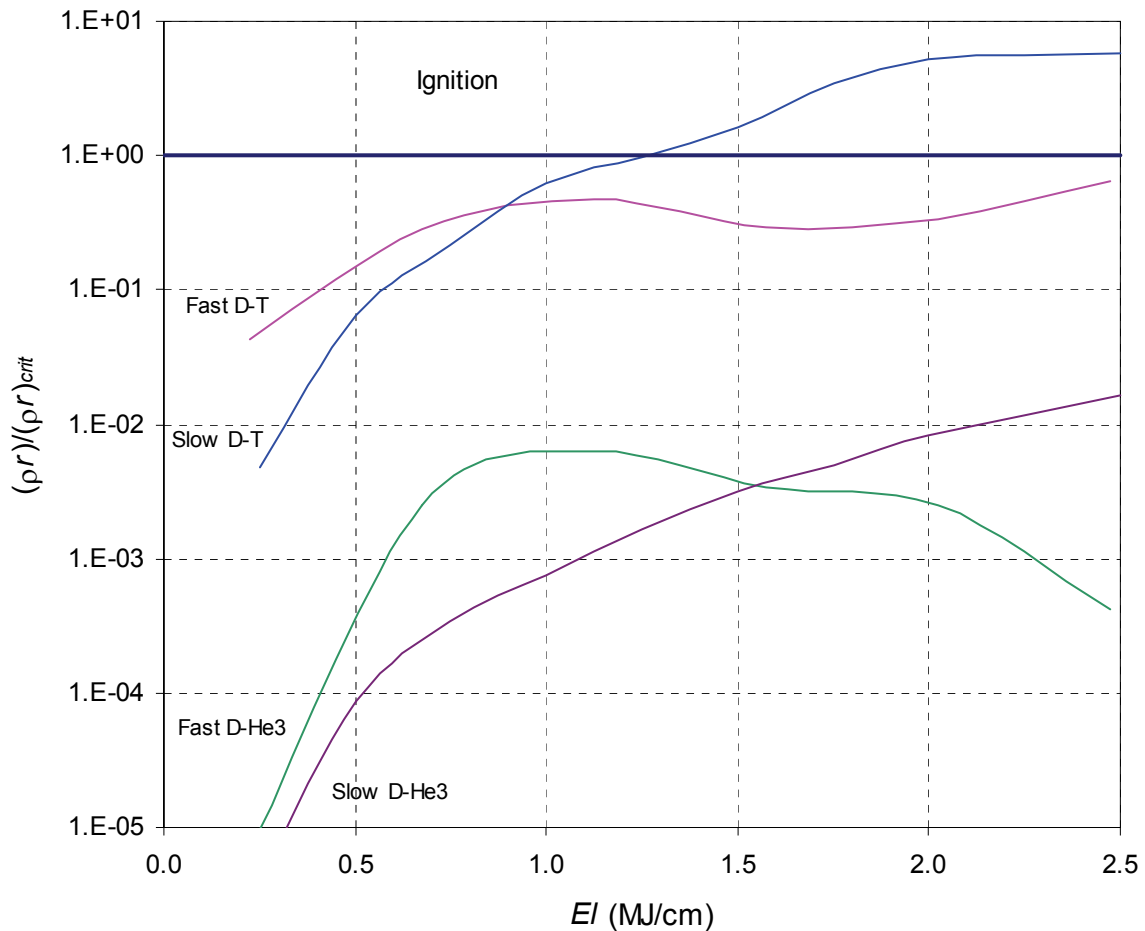

Figure 7. Ignition condition for slow and fast liner for D-D and D-He3 plasma.

Note that for detonation propagation the plasma does not have to be heated to the ignition temperature, and therefore the resulting energy required for detonation is much smaller than that for volume ignition. Provided the spark energy can be neglected with respect to the total energy, the spark ignition scheme is energetically much more advantageous than the volume ignition.

Slow liners can be useful for compressing the plasma up to the detonation propagation condition in both D-T and D-He3. The liner energy required is about 1 MJ/cm. At the same time, the development of the $m = 0$ instability, creates a region where the ignition condition may be reached. At that point a thermonuclear detonation is triggered; it can then propagate along the pinch if the adequate conditions were already achieved. The numerical code can help in finding the best regime to this purpose.

5. Development of the KH instability

Another physical problem studied by means of the numerical code is related to the turbulent mixing layers of plasma at the near equatorial flanks of the terrestrial magnetopause. The numerical 3D code was used to simulate the large amplitude perturbations and waves at the dusk side low latitude boundary layer of the magnetopause generated by an interplanetary tangential discontinuity.

We focused on the motion and structure of the magnetopause/boundary layer observed in response to a joint tangential discontinuity/vortex sheet (TD/VS) observed by the ACE spacecraft on December 7, 2000. Sharp polarity reversals in the east-west components of the field and flow occurred at the discontinuity. These rotations were followed by a period of strongly north-ward IMF. These two factors elicited a two-stage response at the magnetopause, as observed by Cluster spacecraft situated in the boundary layer at the dusk side terminator.
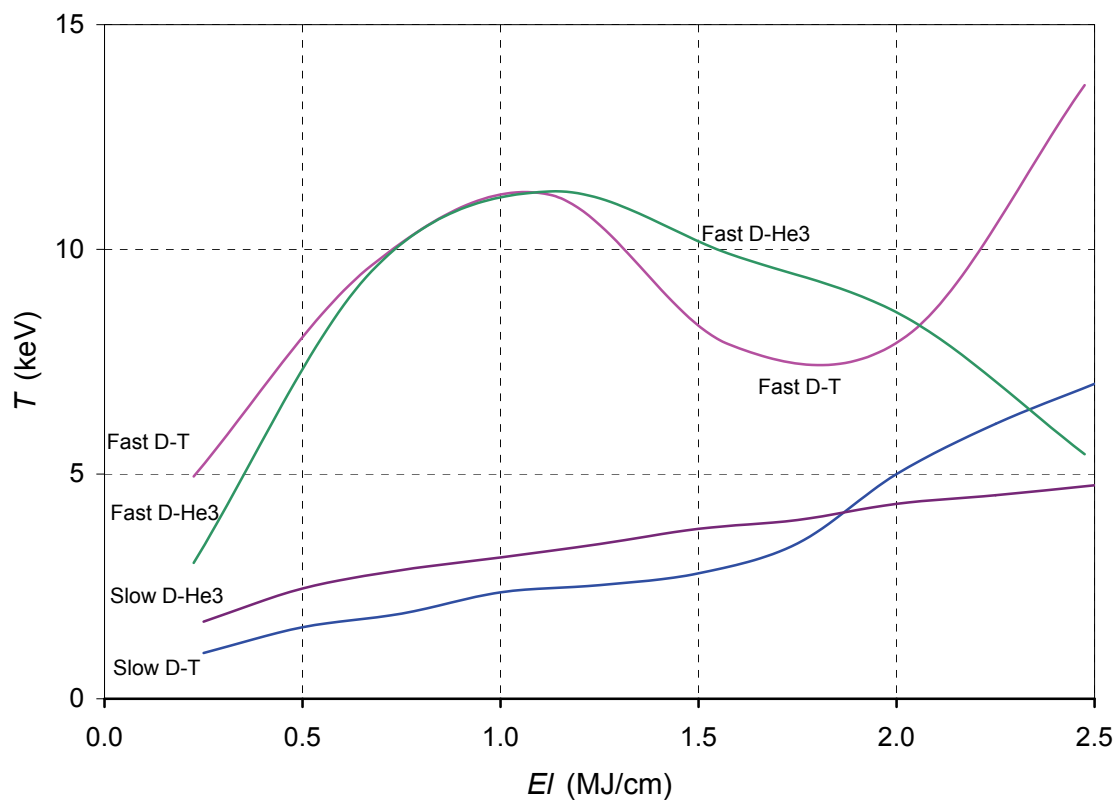

Figure 8. Temperature at the centre of the pinch for slow and fast liner for D-D and D-He3 plasma.

These studies were aimed to clarify some particular physical properties of the instability of velocity shear flows and mixing layers, such as the 3D vorticity amplification mechanism and non conservation of vorticity flux.

The most common of these is the Kelvin-Helmholtz instability feeding on the flow shears which exist across the magnetosheath/magnetosphere interface (see figure 9). Ever since Dungey [21] pointed out the possibility of the magnetopause going Kelvin-Helmholtz unstable, many studies have been devoted to this instability, the surface waves it causes, their coupling to the geomagnetic field giving rise to field line resonances, and how this instability might mediate the entry of magnetosheath plasma into the magnetosphere [22-31].

Attention has been drawn to two other interplanetary parameters whose changes may occasion considerable deformation and motion of the magnetopause. One is a variable orientation of the

interplanetary magnetic field (IMF). Fairfield et al. [32] showed that, even when the dynamic pressure is constant, the magnetopause and inner-magnetosphere boundaries may be in motion. They attributed these motions to pressure changes generated in the foreshock region by the IMF changes. These pressure changes subsequently convect through the bow shock and impinge on the magnetopause. The authors thus concluded that even in the presence of a solar wind that is absolutely steady in velocity and density but which carries an embedded interplanetary magnetic field of variable orientation; there will be a variation of pressure exerted on the magnetopause.
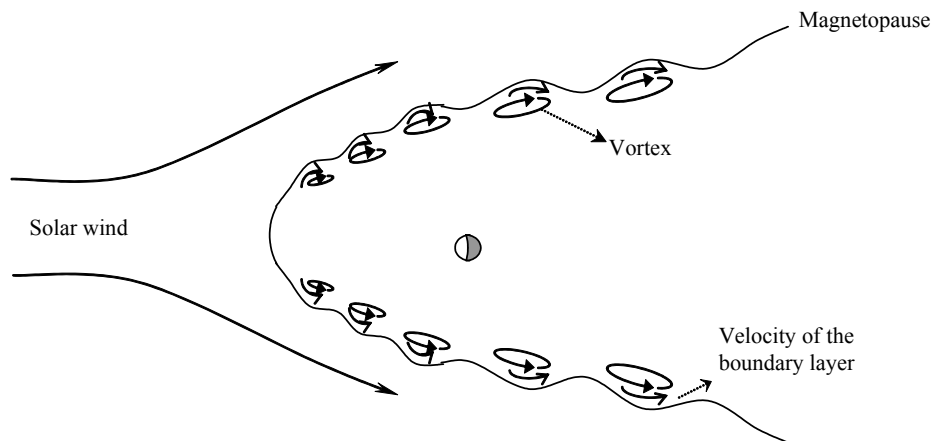

Figure 9. Sketch of vortex formation due to the Kelvin Helmholtz instability in the magnetopause

For the observations at the magnetopause we focused on Cluster 3 data. The Cluster spacecrafts were on an outbound trajectory just tail ward of the dusk terminator and at northern latitudes. (At this early stage of the mission, the spacecraft separation was of order a few hundred km and all spacecraft see the same features.). For some hours prior to our observations, the spacecraft stayed in the vicinity of the magnetopause because the magnetopause boundary was expanding slowly outward due to a slow decrease in dynamic pressure. From 14:00 to 14:30 UT the spacecraft stays within a distance of 0.4 RE from the magnetopause. We may reasonably assume that Cluster 3 is inside the boundary layer according to the model, in agreement with instrument readings.

We carried out a stability analysis of a limited segment of the magnetopause, where the boundary layer may be considered to lie in a local tangent plane. The boundary layer is then modelled as a planar plasma slab with stratified density, flow velocity, and magnetic field. The physical quantities on either side of the magnetosheath-magnetosphere transition are obtained from the Cluster 3 readings at the extremes of the large oscillations recorded after 13:58 UT. Specifically, we selected the second oscillation, where the lowest speed was recorded at maximum T. That is, we assume that at the extremes of the oscillation, Cluster 3 samples alternately the high density-low temperature magnetosheath plasma, and the low density-high temperature magnetosphere plasma. In this way the local instability is examined by parameters measured locally and in temporal proximity.

The full description of the problem and main results are presented in a separated paper in these Proceedings [33]. Anyhow, some sample outputs showing the 3D, complex character of the problem are presented. Figure 10 shows streamlines complexity and formation of a swirling flow in the large eddy at $t = 84$ s. In figure 11 temperature, density, pressure and magnetic lines plots show that the KH waves appear already after a few theoretical e-folding times, due to the great oscillations generated by the tangential discontinuity stress that has reduced the amplification time. In order to get an appropriated resolution, up to 1,000,000 cells were used.
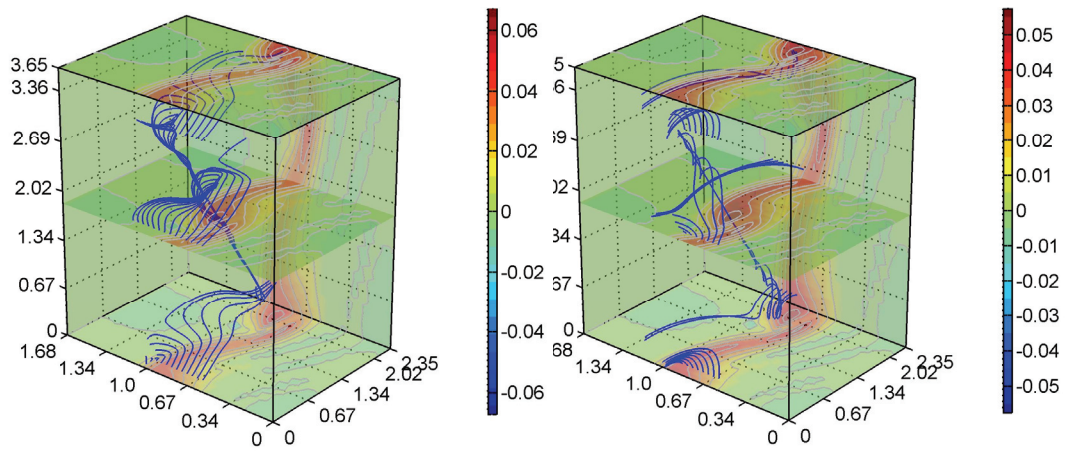
Figure 10. Mixing layer, $t = 84$ s, vorticity contours and streamlines. Comparing streamlines views: left, fixed (Earth) frame, and right, moving frame with average velocity ($U = 78.5$ km/s). In the moving frame magnetosheath and magnetopause plasmas are seen counter streaming.
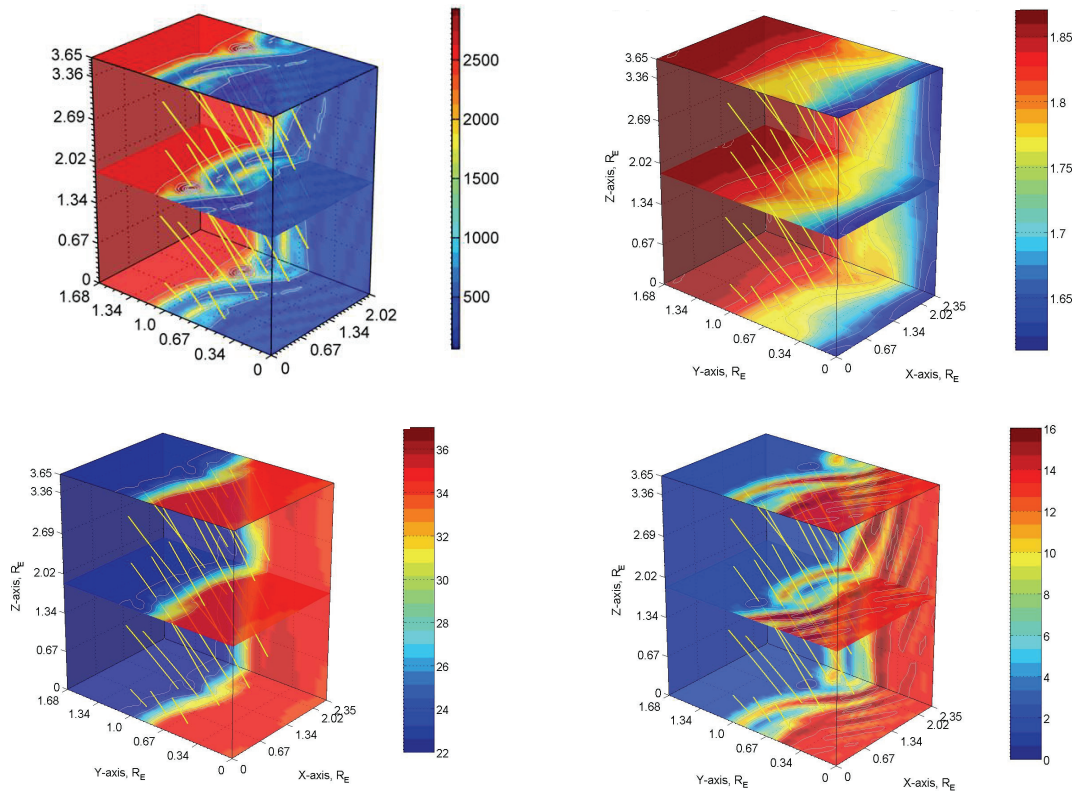

Figure 11. Scalar fields and magnetic lines at $t = 180$ after an e-folding time. Upper left: temperature; upper right, isobars; lower left, |**B**|; lower right, density.

Some interesting features of the phenomenon are obtained from the numerical results. For example, high temperature rises in a compact vortex core correlated with local density depletion while gas, and magnetic pressure (roughly constant across the structure) are near to surrounding values. Also detected

a high density patch in a vorticity structure correlated with a local increase of gas pressure, whereas temperature stays near to surrounding values.

Concomitant with 3-D vortex stretching, kinetic helicity density rises at the vorticity cores. Finally, non conservation of vorticity becomes manifest at about (or even before) one rollover time, where in addition to vortices with positive rotation (the same sign of the original vorticity sheet) other coherent structures with strong negative vorticity also arise.

6. Conclusions

The numerical simulation was a powerful tool for the parametric analysis of pinch compression and development of Kelvin-Helmholtz instability.

The sequential implementation resulted of practical use, because each physical process was treated with a different numerical method.

The improved hydrodynamics method worked well in an ample range of Mach number from subsonic (10^{-3}) to supersonic.

The time step was restricted by efficiency considerations rather than stability conditions. When time step becomes larger, the calculation progress faster because fluid variables, transport properties, etc., are updated with less frequency. But the implicit stage (phase two) of the hydrodynamic advance requires more iterations to perform. An optimum time step has been used for which the minimum computational effort is obtained.

7. Acknowledgments

8. References

[1]   Bilbao L 1990 *J Comp Physics* **91** 361.
[2]   Tonks L 1937 *Trans Electrochem Soc* **72** 167.
[3]   Butler T D, Henins I, Jahoda F C, Marshall J, Morse R L 1969 *Phys Fluids* **12** 1904.
[4]   Gratton F, Vargas M 1976 *Proc. Energy Storage Compression and Switching* (Bostick, Nardi, Zucker Eds Plenum Press).
[5]   Potter D E 1971 *Phys Fluids* **14** 9.
[6]   Maxon S, Eddleman J 1978 *Phys Fluids* **21** 10.
[7]   Gourlan C, Kroegler H, Maisonnier Ch, Rager J.P, Robouch B, Bertalot L, Gentilini A, Arcipiani B, Pedretti E, Steinmetz K 1978 *Proc 2nd Int. Conf on Energy Storage Compression and Switching* (Plenum Press, New York) 221.
[8]   Artsimovich L A 1961 Controlled Nuclear Reactions *Fizmatizdat* Moscow.
[9]   Bakshaev Yu L, Blinov P I, Chernenko A S *et al* 2000 *Czech J Phys* **Suppl 50** (3) 121-126.
[10]   Batunin A V, Bulatoy A N, Vikharev V D 1990 *Fizika Plasmy* (*Sov J of Plasma Physics*) **16** 1027-1035.
[11]   Gol'berg S M, Liberrmann M A, Velikovich A L 1990 *Plasma Phys Contr Fusion* **32** 319-326.
[12]   Ryutoy D D, Derzon M S, Matzen M K 2000 *Reviews of Modern Physics* **72** 167-223.
[13]   Branitski A V *et al* 1996 *Proc Beams 96* Prague 140.
[14]   Quintenz J P and Sandia Team 1998 *Proc Beams 98*.
[15]   Maisonnier Ch *et al* 1965 *Proc Plasma Phys And Contr Nucl Fus Reserch* (IAEA Culham) **Vol 2** 345.
[16]   Bortolotti A *et al* 1993 *Proc 3rd Int Conf On DZP* (London) **AIP 299** 372.
[17]   Degnan J H *et al* 2001 *IEEE Transactions on Plasma Science* **29** 93.
[18]   Avrorin E N, Bunatyan A A, Gadzhiev A D *et al* 1984 *Fiz Plasmy* **10** 514 [*Sov J Plasma Phys* **10** 298].
[19]   Bilbao L, Linhart J G 1996 *Plasma Phys Reports* **22** 457.
[20]   Bosch H S, Hale G M 1992 *Nuclear Fusion* **32** 611.

[21] Dungey J W 1955 "Electrodynamics of the outer atmospheres" Report 69, Ions Res Lab. Pa State Univ, University Park.

[22] Southwood D J 1979 *Proceedings of Magnetospheric Boundary Layers Conference* ESA SP-148 Eur Space Agency Paris 359

[23] Miura A 1984 *J Geophys Res* **89** 801

[24] Chen S H, Kivelson M G, Gosling J T, Walker R J, Lazarus A J 1993 *J Geophys Res* **98** 5727.

[25] Kivelson M G, Chen S H 1995 in *Physics of the Magnetopause* (edited by P Song, B U O Sonnerup and M F Thomsen) *Geophys Monogr Ser* **90** AGU Washington DC 257.

[26] Seon J L, Frank A, Lazarus A J, Lepping R P 1995 *J Geophys Res* **100** (11) 907.

[27] Fairfield D H, Otto A, Mukai T, Kokubun S, Lepping R P, Steinberg J T, Lazarus A J, Yamamoto T 2000 *J Geophys Res* **105** (22),159.

[28] Otto A, Fairfield D H 2000 *J Geophys Res* **105** (A9) 21175-21190.

[29] Farrugia C J, Gratton F T, Contin J, Cocheci J C C, Arnoldy R L, Ogilvie K W, Lepping R P, Zastenker G N, Nozdrachev M N, Fedorov A, Sauvaud J A, Steinberg J T, Rostoker G 2000 *J Geophys Res* **105** (A4) 7639-7667.

[30] Gratton F T, Bender L, Farrugia C J, Gnavi G 2004 *J Geophys Res* **109** (A04211) 1-13.

[31] Farrugia C J, Gratton F T, Torbert R 2001 *Space Sci Rev* **95** (1/2) 443-456

[32] Fairfield D H, Baumjohann W, Paschmann G, Luehr H, Sibeck D G 1990 *J Geophys Res* **95** 3773-3786.

[33] Gratton F T, Bilbao L, Farrugia C J, Gnavi G 2008 "Large eddy simulations in MHD: the rise of counter-rotating vortices at the magnetopause" this *JOP Conf. Series*.